Hindawi
International Journal of Polymer Science
Volume 2022, Article ID 8673245, 16 pages
https://doi.org/10.1155/2022/8673245

Research Article

Influence Mechanism of Rubber Thermal Oxygen Aging on Dynamic Stiffness and Loss Factor of Rubber Isolation Pad

Junjie Chen,[1] **Xian Li**,[1,2] **Changyao Chen**,[1] **Chaofeng Yang**,[3] **and Xiangdong Gao**[1]

[1]*School of Mechanical and Electrical Engineering, Jiangxi University of Science and Technology, Ganzhou 341000, China*
[2]*State Key Laboratory for Modification of Chemical Fibers and Polymer Materials, College of Materials Science & Engineering, Donghua University, Shanghai 201620, China*
[3]*Anhui Zhongding NVH Co., Ltd., Ningguo 242300, China*

Correspondence should be addressed to Junjie Chen; cjj852456@163.com and Xiangdong Gao; gaoxd@jxust.edu.cn

Received 27 July 2022; Accepted 26 September 2022; Published 5 November 2022

Academic Editor: Zhonghua Peng

The influence mechanism of thermal oxygen aging on the dynamic characteristic of the rubber isolation pad (RIP) is usually ignored in studies. However, the ambient temperature of the RIP could reach up to 70°C in general, and even 108°C under some extreme conditions, which will lead to accelerated thermal oxygen aging and a decline in the mechanical performance for the RIP. In the meantime, the thermal oxygen aging will result in excessive vibration and even a damaged external air conditioner. Therefore, the research on the influence mechanism of rubber thermal oxygen aging on the dynamic performances of the RIP is crucial to the mechanical characteristic matching of the RIP. Considering the effect of the thermal oxygen aging on the dynamic characteristic, a novel model of thermal oxygen aging-dynamic characteristic of the RIP is established by adopting the Peck model, the hyperelastic model, the fractional derivative model, and the smooth Coulomb friction model (SCFM) in this paper. A test rig of the static and dynamic characteristics of the RIP is built, and an identification method of model parameters is developed based on the MTS831 elastomer test system as well which of the thermal oxygen aging-dynamic characteristic model is verified by the experimental data. The result is shown that the maximum growth rate of the static stiffness and the dynamic stiffness is 20.7% and 4.5%, respectively, and the maximum decrease rate of the loss factor is 10.6% as the thermal oxygen aging hardness of the RIP increases by 5HA. The amplitude-dependent, frequency-dependent, and thermal oxygen aging-dependent performances of the RIP are effectively characterized by the thermal oxygen aging-dynamic characteristic model. Moreover, a theoretical foundation is provided for the evolution law of the dynamic characteristic of the RIP after the service with the thermal oxygen aging condition in this research.

1. Introduction

The rubber isolation pad (RIP) is the main vibration isolation [1–3] element of the air conditioner compressor, which is widely used in household air conditioners and automotive air conditioners. The RIP is used to fix and support the compressor through the stud of the air conditioner chassis to reduce the horizontal and vertical vibration of the compressor. Thus, the RIP can effectively protect the compressor and the corresponding connection piping, and the RIP also can reduce the noise of the compressor at the same time. In addition, the RIP can effectively prevent the compressor from directly colliding with the bottom plate during transportation. Therefore, the RIPs play a key role in protecting the compressor and vibration attenuation. According to our jointly experimental research with the Midea Group Co., Ltd, the internal temperature of the air conditioner outdoor unit (including the compressor and the RIPs) can reach up to about 108°C during the operation. The thermal oxygen aging phenomenon of the RIP will be generated by the influence of internal temperature [4, 5]. The dynamic characteristic of the RIP will be changed continuously under the thermal oxygen aging condition, which will make the vibration and noise of the compressor and the pipeline of the air conditioner

gradually increase and even damage the pipeline of the air conditioner. Thus, considering the thermal oxygen aging factor, the establishment of the thermal oxygen aging-dynamic characteristic model of the RIP has great theoretical and engineering significance for predicting the vibration performance of household or industrial air conditioners after the service.

To study the dynamic characteristic of the RIP, it is necessary to analyze the static stiffness first, and it is essential to choose a suitable constitutive model to analyze the static force–displacement relationship of the RIP. The Mooney–Rivlin constitutive model [7–10] can be adopted due to the small deformation of the RIP during the operation. Kaya et al. [11] performed modeling analysis and shape optimization on the hyperelasticity of rubber and obtained model parameters of the material constitutive model by fitting the experimental data of the uniaxial tensile test and the planar tensile test. Oza et al. [12] extracted the material constants by using a computer-aided engineering (CAE) method and the uniaxial tension, the uniaxial compression, the bi-axial tension, the planar shear, and the volumetric test of rubber, which provided an effective method for predicting the hyperelasticity behavior of rubber.

The effect of the thermal oxygen aging factors on the rubber materials was not taken into consideration in the above studies, then some scholars began to study the effect of rubber thermal oxygen aging on the mechanical performances [13, 14]. Nie et al. [15] conducted an experimental analysis of the thermal oxygen aging and the mechanical fatigue on natural rubber under the different fillers' matrix, and the aging mechanism of rubber was analyzed from the aspects of crosslink density and defects content, which provided a theoretical basis for modeling the mechanical characteristic of rubber with the thermal oxygen aging condition. Azura et al. [16] studied the effects of different types and filler loading of carbon black on the mechanical, electrical, and aging properties of natural rubber from the material level, and the effect of the thermal oxygen aging on the mechanical properties was investigated under the accelerated aging experiment at a temperature of 100°C.

Considering the influence of carbon black alone, it is not enough to reflect the effect of the thermal oxygen aging on the dynamic characteristic of rubber. Loh et al. [17] established the finite-element model of the air conditioner compressor and the pipeline tested the radial and axial static stiffness and dynamic stiffness of the RIP by using an MTS830 elastomer test system. Then, the prediction method of the stiffness characteristic of the RIP was put forward. However, the test conditions of the dynamic stiffness only included two frequency points of 25 and 47 Hz. The test data are insufficient, and the corresponding mathematical model of the dynamic characteristic has not been established as well. The classical Kelvin–Voigt model, Maxwell model, and three-element solid model are usually used to characterize the frequency dependence of the dynamic characteristic of rubber isolators [18, 19]. Hu et al. [20] superimposed the hyperelastic model, and several generalized Maxwell models, elastoplastic models in parallel, and the model parameters were determined by the uniaxial tensile test, the uniaxial compression test, and the shear test. Then, the validity of the built model was verified by CAE calculations. The results show that the established model can effectively characterize the amplitude dependence and the frequency dependence of the dynamic characteristic. However, the fitting accuracy of the dynamic characteristic needs to be further improved. At the same time, excessive model parameters are difficult to be identified and lack physical significance.

To overcome the defect of insufficient accuracy of the dynamic characteristic models such as the Kelvin–Voigt model and the generalized Maxwell model, the fractional derivative model was used to more accurately characterize the dynamic characteristic of rubber materials. Chen et al. [21, 22] introduced the fractional derivative model and the SCFM to model the convoluted air springs, and the experimental data are in good agreement with the theoretical values. However, the influence factors such as rubber thermal oxygen aging on the dynamic stiffness and the loss factor are not considered, and the dynamic characteristic with the thermal oxygen aging has not been further studied as well.

The above studies of rubber vibration isolators are usually applied in the field of automotive vibration isolation. Few research focuses on the dynamic characteristic of the RIP of the air conditioner compressor, and most of them do not consider the influence of the thermal oxygen aging factor on the dynamic characteristic of the rubber isolation element [23]. Rodas et al. [24] established the thermo-visco-hyperelastic constitutive model, which was verified by the finite-element method. The results have shown that the constitutive model offers satisfactory predictions of both mechanical behavior and self-heating. However, the variation of force–displacement relationship and the influence of rubber thermal oxygen aging are not considered as well. Zhi et al. [25] further considered the effect of the thermal oxygen aging, and then, a suitable constitutive model of aging-viscoelastic coupling was established. However, the influence of the thermal oxygen aging on the dynamic viscoelasticity of natural rubber was only studied by the finite-element method, rather than the accurately theoretical modeling method, which is difficult to be directly applied to stiffness optimization of the vibration isolation system.

The above research has deficiencies as follows: (1) the dynamic characteristic model with sufficient accuracy was not established, and the effect of the thermal oxygen aging was not considered. (2) In the automotive field, the rubber vibration isolators are mainly used as engine mounts, and the ambient temperature, the preload, the operating frequency, etc., are far different from the RIPs. Therefore, a high-precision thermal oxygen aging-dynamic characteristic model should be established to carry out precise stiffness matching of the RIP and improve the quietness of the air conditioner.

The Arrhenius model [26, 27] is introduced since the thermal oxygen-accelerated aging [28, 29] to describe the evolution law of the dynamic characteristic of the RIP. Moreover, the rubber hardness is also introduced to further improve modeling accuracy. The hardness of rubber is proportional to the static stiffness; hence, the Peck model [30] is more suitable because of considering the influence of hardness. The Peck model, the hyperelastic model, the fraction derivative model, and the SCFM are proposed to jointly

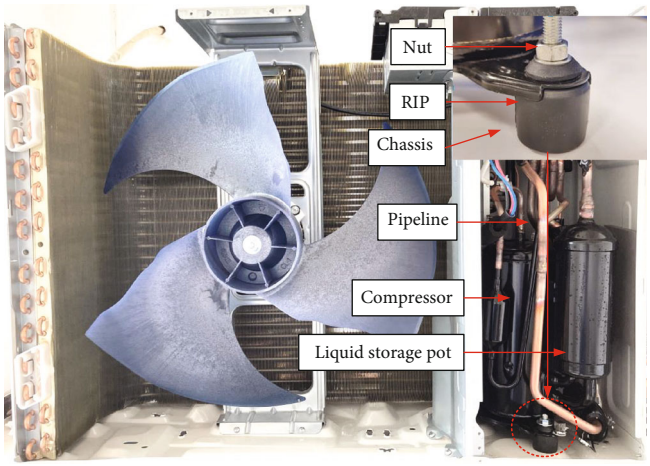

Figure 1: Air conditioner outdoor unit.

establish dynamic characteristic models of the RIP of the compressor under the effect of the thermal oxygen aging. A thermal oxygen aging-dynamic characteristic model with the thermal oxygen aging factor is developed in this paper, and then, the identification methods of thermal oxygen aging-dynamic characteristic model parameters are also put forward. It can predict the dynamic characteristic of the RIP under the influence of the thermal oxygen aging condition and can provide a guide for the stiffness design and matching of the RIP.

This paper is organized as follows, a novel thermal oxygen aging-dynamic characteristic model is proposed in Section 2, the experimental devices and test methods are developed in Section 3, the model parameters are identified, and the novel model is validated by the experimental data in Section 4, and then the conclusions and the outlooks are drawn thereafter.

2. Thermal Oxygen Aging-Dynamic Characteristic Model

The main components of the air conditioner outdoor unit including the RIPs are shown in Figure 1. The operating ambient temperature of the RIPs can continue to increase due to the heat generated during the operation of the compressor. The dynamic characteristic of the RIPs will be degraded by the thermal oxygen aging phenomenon. Therefore, it is necessary to modify the dynamic characteristic model of the RIP by considering the thermal oxygen aging effect to more accurately describe the evolution mechanism of the thermal oxygen aging-dynamic characteristic of the RIP.

The dynamic characteristic of the RIP is affected by the excitation frequency, the excitation amplitude, and the thermal oxygen aging condition, etc. As shown in Figure 2, based on the hyperelastic model, the fractional derivative model, the SCFM, and the thermal oxygen aging factor, a novel thermal oxygen aging-dynamic characteristic model of the RIP is established in this paper.

In Figure 2, K_{he}, K_v, and K_f are the equivalent elastic stiffness, the stiffness of the fractional derivative Kelvin–Voigt model (abbreviated as FDKVM), and the stiffness of the SCFM, and μ and β are the thermal oxygen aging factor and the material parameter, respectively.

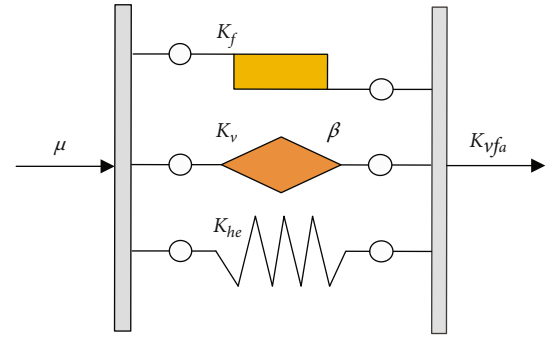

Figure 2: Thermal oxygen aging-dynamic characteristic model of RIP.

Based on the linear elastic model, the hyperelastic model is applied to accurately describe the relationship between the non-linear force and the displacement of the RIP [31]. In the field of railway vehicle vibration reduction, the fractional derivative standard model can well characterize the frequency dependence of the RIP with fewer parameters. Thus, the FDKVM composed of the hyperelastic model, and the fractional derivative standard model is established to better describe the viscoelastic properties of the RIP [32]. Furthermore, the amplitude dependence of the RIP can be characterized by the SCFM, and then, the thermal oxygen aging factor is developed based on the peck model in this paper.

In this paper, the Peck model is used to represent the thermal oxygen aging of the RIP, so the degradation behavior of the dynamic characteristic can be predicted. The Peck model can be expressed as follows [30]:

$$Q(T) = C_1 \mathrm{HA} e^{E_a/RT}, \tag{1}$$

where $Q(T)$ is the reaction rate, HA is the Shore hardness, C_1 is the acceleration coefficient with the thermal oxygen aging, E_a is the activation energy of the reaction, R is the molar gas constant, and T is the Kelvin temperature. Based on the Peck model, the thermal oxygen aging factor of the RIP can be described as below:

$$\mu = 1 + C_1 \mathrm{HA} e^{-E_a/RT} t, \tag{2}$$

where μ is the thermal oxygen aging factor, and t is the thermal oxygen aging time.

The finite-element analysis (FEA) is combined to establish the hyperelastic model, and the dynamic characteristics of the RIP with or without thermal oxygen aging are analyzed theoretically and experimentally, which lay a foundation for matching and optimizing the stiffness of the RIP. The overall research procedure is shown in Figure 3.

The left part of Figure 3 is the thermal oxygen aging-dynamic characteristic model of the RIP, the upper right part is the process of establishing the dynamic characteristic model without the thermal oxygen aging, and the lower right part is the parameters identification of the thermal oxygen aging factor. The specific steps of Figure 3 are as follows:

(1) Dumb-bell test pieces were made.

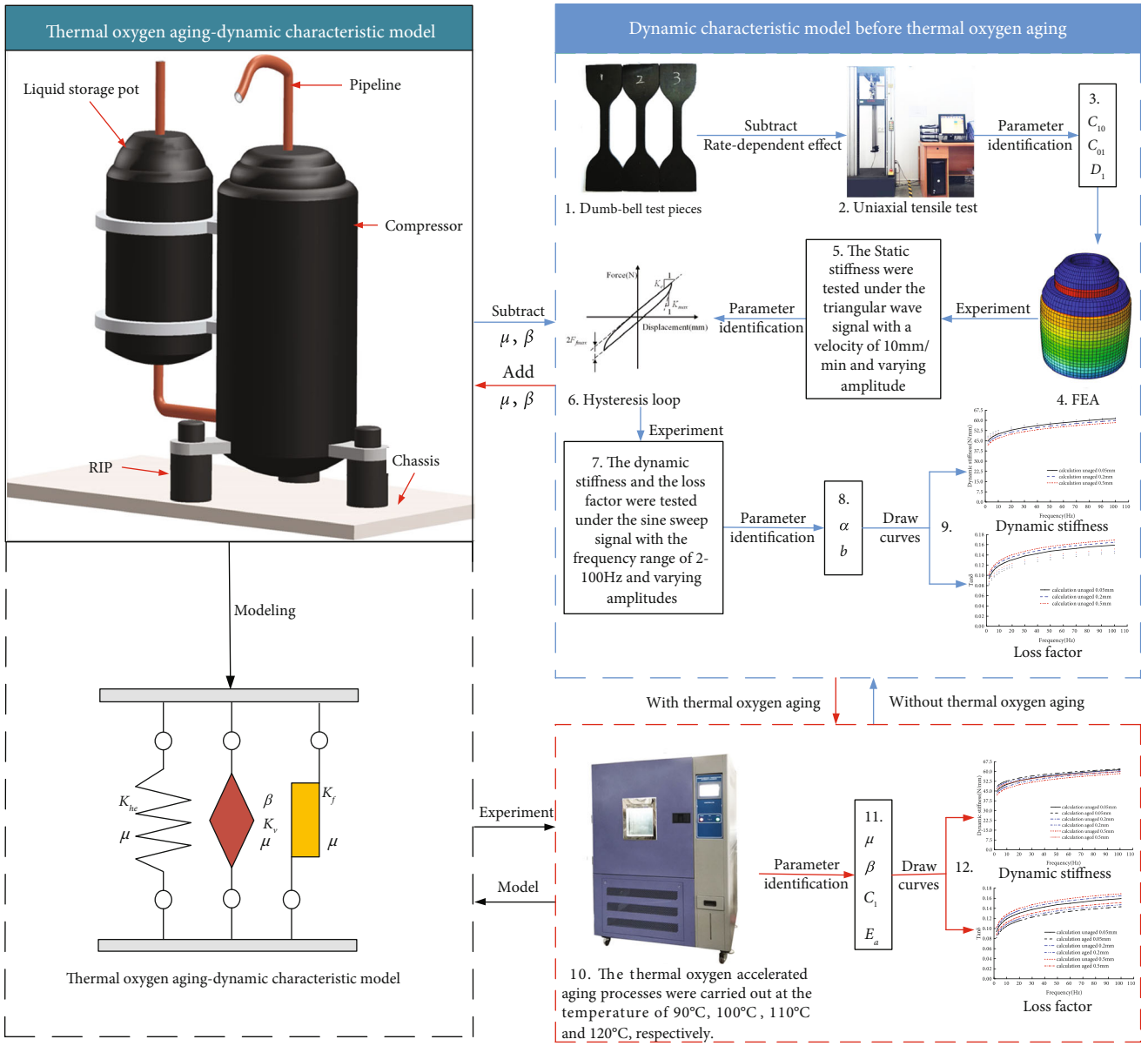

Figure 3: Schematic diagram of the thermal oxygen aging-dynamic characteristic model.

(2) The dumb-bell test pieces were subjected to the uniaxial tensile test.

(3) Then, the parameters of C_{10}, C_{01}, and D_1 were identified by the experimental data of the uniaxial tensile.

(4) The FEA model of the RIP based on the identified parameters of C_{10}, C_{01}, and $D_1$was built.

(5) The static stiffness was tested under the amplitudes of 0.2, 0.5, 1 mm, and the loading velocity of 10 mm/min.

(6) Based on the experimental data of the static stiffness, the hysteresis loop was used to identify the parameters of K_e, F_{fmax}, and K_{max}. Then, the experimental values of the static stiffness and FEA results were combined to establish the hyperelastic model.

(7) The dynamic stiffness test was performed under the amplitudes of 0.05, 0.2, 0.5 mm and the frequency range of 2–200 Hz, and the interval of 2 Hz.

(8) The model parameters of α and b were obtained by applying the least square method.

(9) The experimental and calculation curves of the dynamic characteristic for the RIP without the thermal oxygen aging were compared, and the maximum relative error of the comparison curves must be less than 15%. Otherwise, return to step 6.

(10) The thermal oxygen accelerated aging test of the RIPs were conducted under the temperature of 90°C, 100°C, 110°C, and 120°C, respectively.

(11) The remaining parameters of μ, β, C_1, and E_a of thermal oxygen aging-dynamic characteristic model were identified.

(12) The dynamic characteristic curves of the RIP with the thermal oxygen aging were drawn and further compared, and the maximum relative error of the comparison curves must be less than 15%. Otherwise, return to step 11.

2.1. Hyperelastic Model. Without regard to the thermal oxygen aging, the force and displacement of the hyperelastic model of the RIP can be expressed as below:

$$F_{\mathrm{he}} = K_{\mathrm{he}} x, \tag{3}$$

where K_{he} is the equivalent elastic stiffness, $K_{\mathrm{he}} = K_{\mathrm{e}} + K_{\mathrm{c}}$. K_{e} is the linear elastic stiffness, and K_{c} is the correction stiffness. The Mooney–Rivlin constitutive model can better simulate the mechanical behavior of the RIP due to the small strain during the operation of the compressor, and the strain energy function can be expressed as below [33]:

$$W = \sum_{i+j=1}^{N} C_{ij}(I_1 - 3)^i (I_2 - 3)^j + \sum_{K=1}^{N} \frac{1}{d_k}(I_3 - 1)^{2k}, \tag{4}$$

where I_1, I_2, and I_3 are the strain invariants, and C_{ij}, d_k, and N are the material constants.

Since the rubber material is incompressible, the binomial third-order expansion of equation (4) can be written as:

$$W = C_{10}(I_1 - 3) + C_{01}(I_2 - 3). \tag{5}$$

The relationship between the Kirchhoff stress tensor (t_{ij}) and the Green strain tensor (γ_{ij}) can be obtained as follows:

$$t_{ij} = \frac{\partial W}{\partial I_1}\frac{\partial I_1}{\partial \gamma_{ij}} + \frac{\partial W}{\partial I_2}\frac{\partial I_2}{\partial \gamma_{ij}} + \frac{\partial W}{\partial I_3}\frac{\partial I_3}{\partial \gamma_{ij}}. \tag{6}$$

The relationship between the principal stress t_{i} of rubber material and the principal elongation ratio λ_i can be expressed as below:

$$t_i = 2\left(\lambda_i^2 \frac{\partial W}{\partial I_1} + \frac{1}{\lambda_i^2}\frac{\partial W}{\partial I_2}\right) + P, \tag{7}$$

where P is the arbitrary hydrostatic pressure.

For the uniaxial tension, there are $t_2 = t_3 = 0$ and $\lambda_2^2 = \lambda_3^2 = 1/\lambda_1$. For the incompressible materials, there are $I_3 = \lambda_1^2\lambda_2^2\lambda_3^2 = 1$ and $D_1 = 0$. So:

$$\frac{\partial W}{\partial I_1} = C_{10}, \frac{\partial W}{\partial I_2} = C_{01}. \tag{8}$$

Then, Equation (9) can be derived from Equations (7) and (8) as follows:

$$\frac{t_1}{2\left(\lambda_1^2 - 1/\lambda_1\right)} = C_{10} + \frac{C_{01}}{\lambda_1}. \tag{9}$$

2.2. Frequency-Dependent Model. The relationship between the viscous force and the displacement of the fractional derivative standard model can be expressed as below:

$$F_{kv} = bD^{\alpha}x, \tag{10}$$

where a is the fractional derivative order, b is the fractional derivative damping parameter, and D^a represents the fractional differential form. The FDKVM consists of the hyperelastic model and the fractional derivative model in parallel. The force versus the displacement relationship of the FDKVM can be expressed as below:

$$F_{v0} = K_{he}x + bD^{\alpha}x. \tag{11}$$

The dynamic stiffness and the loss angle can be obtained by the Fourier transform of Equation (11):

$$K_v = \sqrt{\left[K_{he} + b\omega^a \cos\left(\frac{a\pi}{2}\right)\right]^2 + \left[b\omega^a \sin\left(\frac{a\pi}{2}\right)\right]^2}, \tag{12}$$

$$\delta_0 = \arctan\frac{b\omega^a \sin(a\pi/2)}{K_{he} + b\omega^a \cos(a\pi/2)}. \tag{13}$$

2.3. Amplitude-Dependent Model. The amplitude dependence of carbon black-filled rubber is like the friction relationship, and the SCFM is used to describe the amplitude dependence. The relationship between the smooth Coulomb friction force of F_{f} and the displacement of x can be expressed as below [34]:

$$F_{\mathrm{f}} = \begin{cases} F_{\mathrm{fs}} & x = x_{\mathrm{s}} \\ F_{\mathrm{fs}} + \dfrac{x - x_{\mathrm{s}}}{x_2(1-\varepsilon) + (x - x_{\mathrm{s}})}\left(F_{\mathrm{fmax}} - F_{\mathrm{fs}}\right) & x > x_{\mathrm{s}} \\ F_{\mathrm{fs}} + \dfrac{x - x_{\mathrm{s}}}{x_2(1+\varepsilon) - (x - x_{\mathrm{s}})}\left(F_{\mathrm{fmax}} + F_{\mathrm{fs}}\right) & x < x_{\mathrm{s}} \end{cases}, \tag{14}$$

where F_{fs} and x_{s} are the reference starting points of the force and the displacement, respectively, and $(F_{\mathrm{fs}}, x_{\mathrm{s}}) = (0, 0)$. $\varepsilon = F_{\mathrm{fs}}/F_{\mathrm{fmax}}$, $\varepsilon \in [-1, 1]$. When reaching half of the maximum friction force, the hyperelastic stiffness K_{he}, the maximum friction force F_{fmax}, and the corresponding displacement x_2 satisfy the following formula:

$$x_2 = \frac{F_{\mathrm{fmax}}}{K_{\mathrm{max}} - K_{\mathrm{he}}}, \tag{15}$$

where K_{max} is the maximum slope of the displacement at both ends of the hysteresis loop. The stiffness K_{f} and the loss

angle δ_1 of the SCFM can be expressed as below:

$$K_f = \frac{F_{fmax}}{2x_2x_0}\left(\sqrt{x_2^2 + x_0^2 + 6x_2x_0} - x_2 - x_0\right), \tag{16}$$

$$\delta_1 = \arcsin\frac{E_f}{\pi F_{f0}x_0}, \tag{17}$$

$$E_f = 2F_{fmax}\left[2x_0 - x_2(1+a_0)^2\ln\frac{x_2(1+a_0)+2x_0}{x_2(1+a_0)}\right], \tag{18}$$

where $a_0 = F_{f0}/F_{fmax}$, x_0 is the excitation amplitude, and $F_{f0} = F_{fmax}(\sqrt{x_2^2 + x_0^2 + 6x_2x_0} - x_2 - x_0)/(2x_2)$.

2.4. Dynamic Characteristic Model of the RIP. Combining Equations (12) and (13) with Equations (16) and (17), the dynamic stiffness and the loss factor of the RIP irrespective of the thermal oxygen aging can be expressed as below:

$$K_{vf} = K_f\cos\delta_1 + K_v\cos\delta_0 + j[K_f\sin\delta_1 + K_v\sin\delta_0], \tag{19}$$

$$K_{vf}^* = \sqrt{[K_f\cos\delta_1 + K_v\cos\delta_0]^2 + [K_f\sin\delta_1 + K_v\sin\delta_0]^2}, \tag{20}$$

$$\tan\delta = \frac{K_f\sin\delta_1 + K_v\sin\delta_0}{K_f\cos\delta_1 + K_v\cos\delta_0}, \tag{21}$$

where j is an imaginary unit, and $j^2 = -1$. K_{vf} is the complex stiffness of the RIP without thermal oxygen aging, K_{vf}^* is the dynamic stiffness of the RIP without the thermal oxygen aging, and tanδ is the loss factor of the RIP without the thermal oxygen aging.

2.5. Thermal Oxygen Aging-Dynamic Characteristic Model of the RIP. Considering the thermal oxygen aging-dependence, the force versus the displacement relationship of the hyperelastic model taking into account the thermal oxygen aging factor μ can be expressed as below:

$$F_{kea} = \mu K_{he}x. \tag{22}$$

Hu et al. [20] introduced several material parameters to describe the change of the viscoelastic force more accurately under the thermal oxygen aging, but it is difficult to identify these parameters due to too many parameters. To simplify the parameters and accurately characterize the viscoelastic changes of the RIP under the thermal oxygen aging, only the linear parameter β is introduced in this paper, and the relationship between the force and the displacement of the fractional derivative standard model can be expressed as below:

$$F_{kva} = \beta\mu bD^\alpha x. \tag{23}$$

Therefore, the relationship between the force and the displacement of the FDKVM considering the thermal oxygen aging factor can be rewritten as follows:

$$F_{va} = \mu(K_{he} + \beta bD^\alpha)x. \tag{24}$$

Through Fourier transform of Equation (24), the dynamic stiffness, and the loss angle of the FDKVM can be obtained as below:

$$K_{va} = \sqrt{\left[\mu K_{he} + \beta\mu b\omega^a\cos\left(\frac{a\pi}{2}\right)\right]^2 + \left[\beta\mu b\omega^a\sin\left(\frac{a\pi}{2}\right)\right]^2}, \tag{25}$$

$$\delta_{a0} = \arctan\frac{\beta\mu b\omega^a\sin(a\pi/2)}{\mu K_{he} + \beta\mu b\omega^a\cos(a\pi/2)}. \tag{26}$$

Similarly, the relationship between the force and the displacement of the SCFM considering the thermal oxygen aging factor also can be rewritten as below:

$$F_f = \begin{cases} \mu F_{fs} & x = x_s \\ \mu\left[F_{fs} + \dfrac{x - x_s}{x_2(1-\varepsilon) + (x - x_s)}(F_{fmax} - F_{fs})\right] & x > x_s \\ \mu\left[F_{fs} + \dfrac{x - x_s}{x_2(1+\varepsilon) - (x - x_s)}(F_{fmax} + F_{fs})\right] & x < x_s \end{cases}. \tag{27}$$

Then, the stiffness K_{fa} and the loss angle δ_{a1} of the corresponding SCFM can be expressed as below:

$$K_{fa} = \mu K_f, \tag{28}$$

$$\delta_{a1} = \arcsin\frac{E_{fa}}{\pi\mu F_{f0}x_0}. \tag{29}$$

From the above, the complex stiffness, the dynamic stiffness, and the loss factor of the RIP with the thermal oxygen aging can be expressed as below:

$$K_{vfa} = K_{fa}\cos\delta_{a1} + K_{va}\cos\delta_{a0} + j[K_{fa}\sin\delta_{a1} + K_{va}\sin\delta_{a0}], \tag{30}$$

$$K_{vfa}^* = \sqrt{[K_{fa}\cos\delta_{a1} + K_{va}\cos\delta_{a0}]^2 + [K_{fa}\sin\delta_{a1} + K_{va}\sin\delta_{a0}]^2}, \tag{31}$$

$$\mathrm{Tan}\delta_a = \frac{K_{fa}\sin\delta_{a1} + K_{va}\sin\delta_{a0}}{K_{fa}\cos\delta_{a1} + K_{va}\cos\delta_{a0}}. \tag{32}$$

where K_{vfa} is the complex stiffness of the RIP with the thermal oxygen aging, K_{vfa}^* and tanδ_a are the dynamic stiffness and the loss factor of the RIP with the thermal oxygen aging, respectively.

3. Experimental Devices and Methods

The experimental equipment in this paper consists of the MTS microcomputer-controlled electronic universal testing

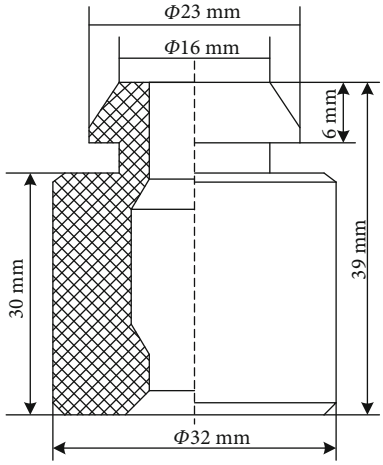

Figure 4: The structure of the RIP.

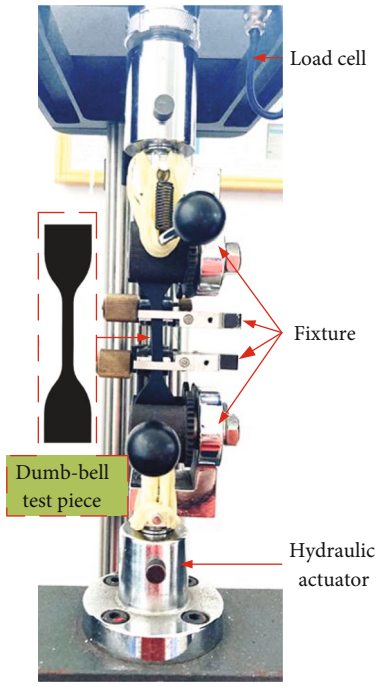

Figure 5: Uniaxial tensile test device.

machine, the MTS831 elastomer test bench, the RIPs (produced by a cooperative enterprise, using Ethylene Propylene Diene Monomer (EPDM) as the main raw material, which has excellent aging resistance, ozone resistance, sunlight resistance, heat resistance, water resistance, and other aging properties and can be used in the temperature range of −40°C to 130°C for a long time. The structure and related dimensions of the RIP are shown in Figure 4), the programmable temperature-humidity test chamber, the fixtures, etc.

3.1. Uniaxial Tensile Test. The uniaxial tensile tests were carried out by the MTS microcomputer-controlled electronic universal testing machine as shown in Figure 5. The specific steps of the uniaxial tensile test were as follows based on the ISO 37: 2005 [35] (Rubber, vulcanized or thermoplastic-

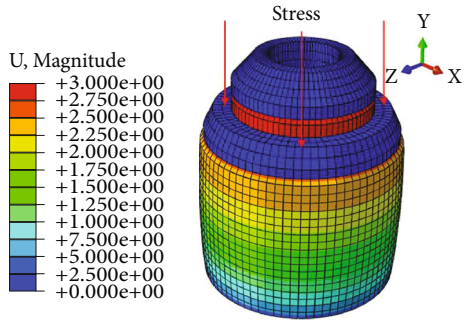

Figure 6: FEA model of the RIP.

determination of tensile stress-strain properties): (1) the fixture related to the MTS microcomputer-controlled electronic universal testing machine. (2) the position of the limit block was adjusted according to the position of the fixture, which can protect the sensor and the fixture from damage. (3) the dumb-bell test piece was clamped to the fixture, then the dumb-bell test piece was stretched at a speed of 500 mm/min. (4) the dumb-bell test piece was loaded to a constant strain value of 3.0, and then it was unloaded to the initial position. The loading–unloading cycles have been repeated three times, and the third results were recorded (due to the Mullins effect).

According to the identified material parameters of the Mooney–Rivlin model, the material properties of the RIP were defined in ABAQUS. The compression displacement was set to 3 mm, calculation results of the RIP are shown in Figure 6.

3.2. Accelerated Thermal Oxygen Aging Experiment. First, the thermal oxygen aging temperatures of the RIPs were set to 90°C, 100°C, 110°C, and 120°C, respectively, and the accelerated thermal oxygen aging process was strictly implemented in accordance with the ISO 188-2011 [36] (Rubber, vulcanized or thermoplastic-accelerated aging and heat resistance tests).

Second, according to the actual engineering applications, the Shore hardness variation of 5HA was set as the critical point for the accelerated thermal oxygen aging.

Third, to avoid the differences of each RIP due to uneven rubber mixing and process difference, 98 RIPs with the same batch vulcanization and the same hardness of 32HA were selected. Two RIPs without thermal oxygen aging were taken out, and the remaining 96 RIPs were equally divided into 4 groups. Each group was put into the test chamber under the temperature of 90°C, 100°C, 110°C, and 120°C, respectively, as shown in Figure 7 (such as 120°C). The compression deformation under the thermal aging process is simulated by attaching preload to the RIP through bolt clamping and limit block.

3.3. Hardness Test. During the accelerated thermal oxygen aging experiment, two RIPs were taken out from each test temperature every 24 hours, and the RIPs were placed at the room temperature for 24 hours, then the hardness of the RIPs was tested with the Shore durometer. The hardness

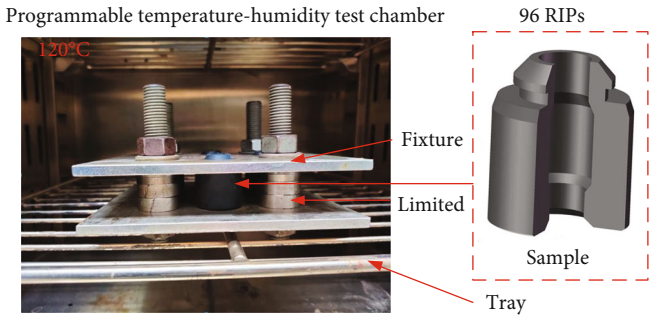

Figure 7: Thermal oxygen aging experiment graph of the RIPs at the temperature of 120°C.

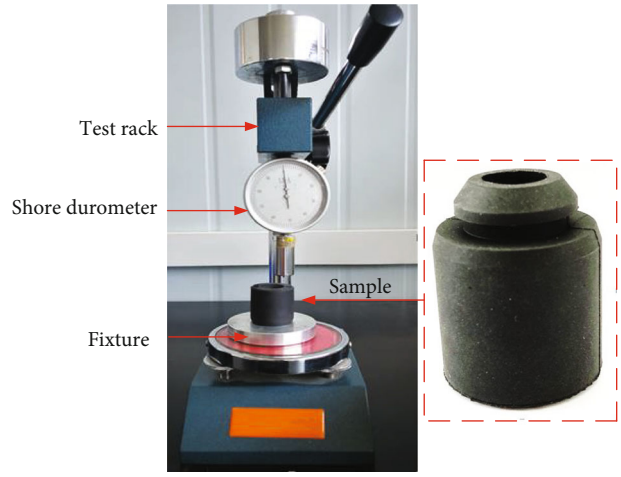

Figure 8: Test rig of hardness.

Table 1: Thermal oxygen aging time under different temperatures.

Temperature/°C	Unaged	90	100	110	120
Hardness/HA	32	37	37	37	37
Aging time/h	—	216	96	48	24

test was performed in accordance with the ISO 7619-1: 2010 [37] (Rubber, vulcanized or thermoplastic-Determination of indentation hardness-Part 1: Durometer method (Shore hardness), as shown in Figure 8.

The experiment was terminated when the hardness of the samples changed by 5HA, and the results of the accelerated thermal oxygen aging time at each test temperature are shown in Table 1.

3.4. Static and Dynamic Stiffness Experiment. The static and dynamic stiffness of the RIPs were tested by the MTS831 elastomer test bench, and the experimental device is shown in Figure 9. Because 98 RIPs were manufactured in the same batch, the difference among the RIPs is small and can be ignored under the same thermal oxygen aging conditions. The static stiffness and the dynamic stiffness tests were carried out for both sample 1# (without the thermal oxygen aging) and sample 2# (with thermal oxygen aging). During the experiment, a preload of 37 N was exerted according to the weight distribution of the compressor, a triangle wave signal with a speed of 10 mm/min and amplitudes of 0.2, 0.5, and 1 mm, respectively, were exerted to test the static stiffness, and a sine sweep signal with the amplitudes of 0.05, 0.2, 0.5 mm, the frequency range of 2–100 Hz, and the interval of 2 Hz were exerted to test the dynamic stiffness.

4. Parameter Identification and Model Validation

4.1. Parameter Identification

4.1.1. Hyperelastic Parameters Identification. The stress value (t_1) can be measured under the different stretch ratios (λ_1) according to the uniaxial tensile test, and then $1/\lambda_1$ was applied as the abscissa and $t_i/2(\lambda_1^2 - 1/\lambda_1)$ was applied as the ordinate. The test points were drawn to form a new curve in the coordinate system, and the curve was regressed into a straight line. Then, C_{10} is the intercept of this line and C_{01} is the slope of this line, the identified parameters are shown in Table 2. As shown in Figure 10, the results show that the stress–strain curves calculated by the fitting parameters (C_{01}, C_{10}) can well reproduce the experimental data.

According to the obtained material parameters of the Mooney–Rivlin model and the established FEA model (Figure 6), the force–displacement curves of the RIP are obtained as shown in Figure 11, and the nonlinear correction stiffness is obtained as shown in Equation (33). It can be seen from Figure 11 that the results obtained by using the hyperelastic model are closer to the experimental data with respect to those obtained by using the linear elastic material model. The larger errors are mainly concentrated in the interval of −0.8 to −1.0 mm and 0.8 to 1.0 mm. The absolute error values are shown in Table 3.

$$K_c = 0.134x^3 - 3.2816x^2 + 0.5447x. \quad (33)$$

4.1.2. Parameters Identification of the Peck Model. Hypothetically, the RIPs are uniformly aging under the thermal oxygen aging process of each test temperature, and the thermal oxygen aging mechanism is the same as well [38]. Thus, the activation energy E_a of the reaction remains unchanged, and the specific identification method of E_a is shown in reference [26]. From Equation (1), the reaction rate ratio at the different temperatures can be expressed as

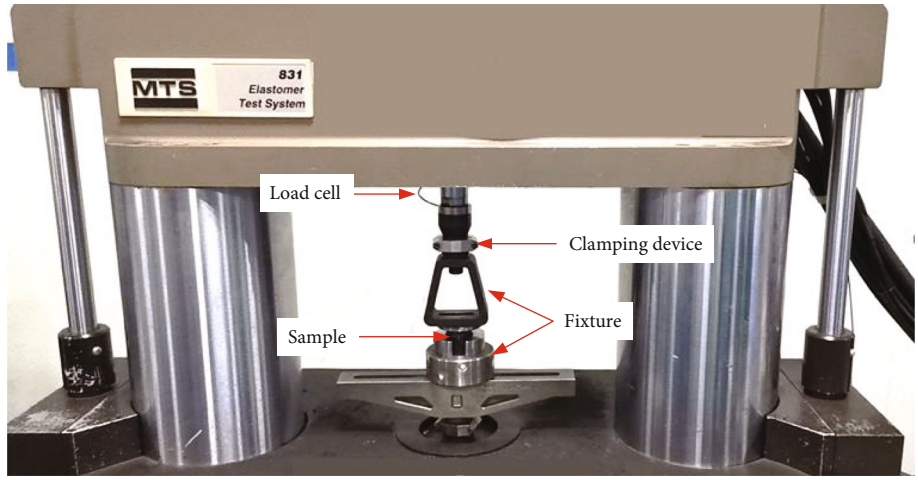

Figure 9: Test rig of the static stiffness and the dynamic stiffness.

Table 2: Values of C_{10}, C_{01}, and D_1.

C_{10}/MPa	C_{01}/MPa	D_1/MPa
0.231147	−0.02274	0

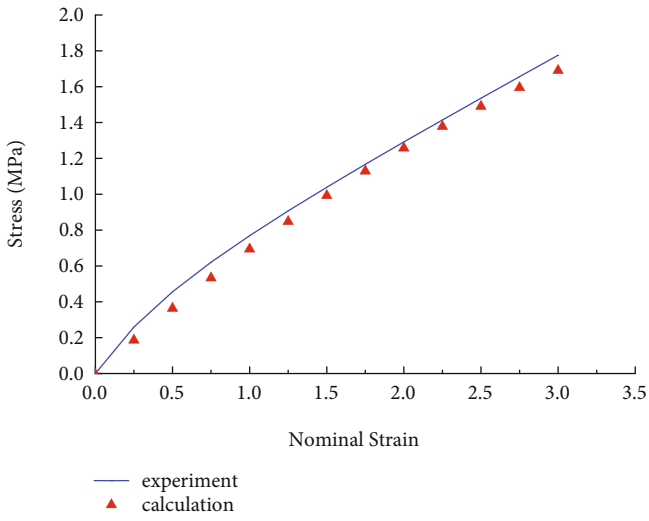

Figure 10: Mooney–Rivlin material parameters fitting curve.

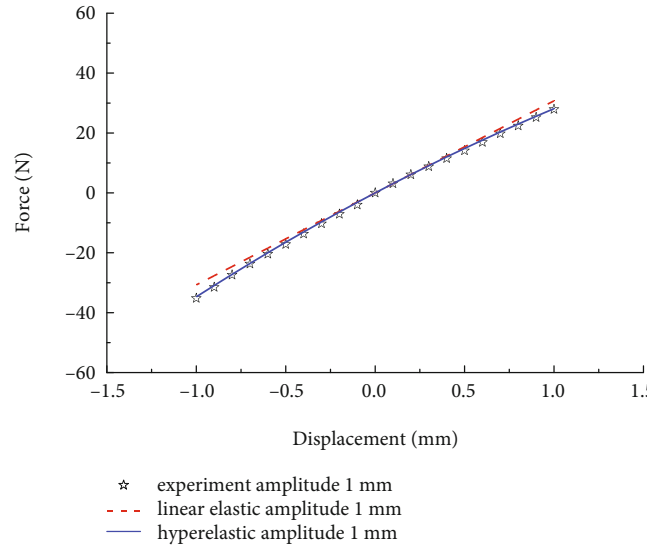

Figure 11: RIP force–displacement curve.

below [39]:

$$\ln q = \frac{E_a}{R}\left(\frac{1}{T_0} - \frac{1}{T}\right), \tag{34}$$

where $q = t_0/t_a$, t_0 is the thermal oxygen aging time at the reference temperature of 90°C, and t_a is the thermal oxygen aging time at the temperature of 100°C, 110°C, and 120°C, respectively. Then, the reaction rate ratio at the different temperatures is shown in Table 4.

Then, the fitting curve of ln$q$ and $1/T$ can be obtained, as shown in Figure 12.

Figure 12 shows that the linear relationship of ln$q$ and $1/T$ at the temperature of 90°C, 100°C, 110°C, and 120°C is very good, which indicates that the thermal oxygen aging mechanism is the same at each test temperature. Thus, the activation energy E_a at each test temperature is consistent, which verifies the correctness of the previous hypothesis as well.

The activation energy E_a can be obtained [39] by the linear line of ln$q$ and $1/T$. Equations (2), (22) and (25) were also combined to obtain the acceleration coefficients C_1, and then these parameters are shown in Table 5.

4.1.3. Parameters Identification of the SCFM and the FDKVM. To minimize the influence of viscous force on RIP, the loading frequency should be reduced as far as possible during the static stiffness test, so that the Coulomb friction can play a major role. Therefore, a triangular wave excitation signal with the loading speed of 10 mm/min, and an amplitude of 1 mm was exerted on the RIP by the MTS831 elastomeric test bench. The static stiffness of the RIP depends on the hyperelastic model and SCFM. The effect of the viscous force can be ignored due to the low

Table 3: Absolute error between calculation and experimental values of two models.

Dispacement (mm)	−1.0	−0.9	−0.8	0	0.8	0.9	1.0
Linear elastic model absolute error (N)	4.5	3.8	2.8	0	2.2	2.5	2.8
Hyperelastic model absolute error (N)	0.5	0.6	0.2	0	0.6	0.4	0.2

Table 4: The reaction rate ratio at the different temperature.

Temperature (°C)	90	100	110	120
q	1	2.25	4.5	9

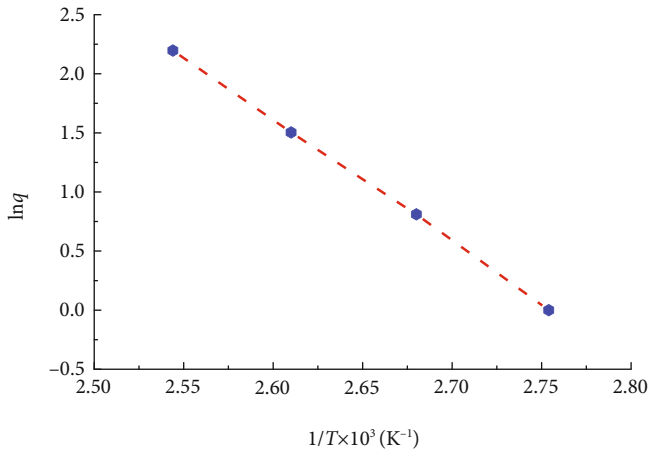

Figure 12: Regression and extrapolation results of the activation energy.

Table 5: Parameters of Peck model.

Symbol	Value	Units
C_1	1.68×10^4	s^{-1}
R	8.314	J/Mol.K
E_a	86.507	kJ/Mol

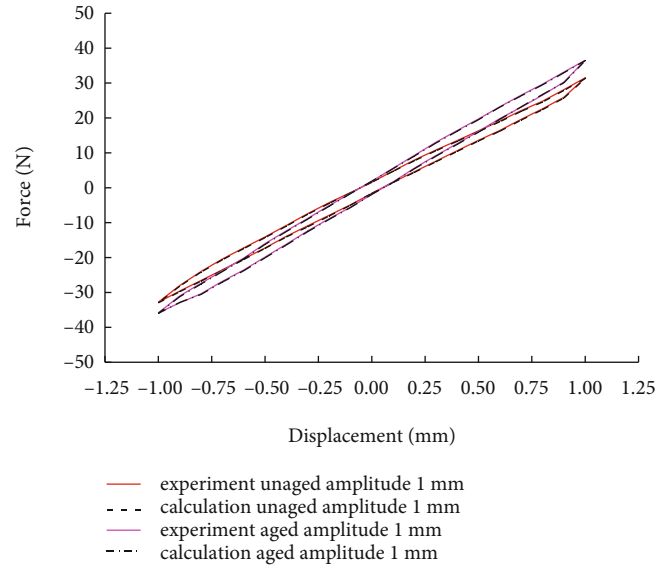

Figure 13: Hysteresis loop with and without thermal oxygen aging (excitation amplitude 1 mm).

Table 6: Model Parameters of the SCFM and the FDKVM.

Parameter	Value	Unit
K_e	32	N/mm
K_c	Equation (33)	N/mm
x_2	0.122	mm
F_{fmax}	1.59	N
α	0.212	—
b	7.488	Ns^a/mm
β	0.815	—

frequency of the static stiffness test. As shown in reference [21, 40] for the parameter identification method of the SCFM, K_e, F_{fmax}, and K_{max} can be identified by the hysteresis loop, the hysteresis loops obtained by the experimental data and calculation values of the RIP with or without thermal oxygen aging are shown in Figure 13.

From Figure 13, the hysteresis loops of the RIP with thermal oxygen aging are inclined upward, and the maximum growth rate of the static stiffness is 20.7% when the thermal oxygen aging hardness increases by 5HA. Compared the hysteresis loop with thermal oxygen aging with that without thermal oxygen aging of the RIP, the experimental data and calculation values are in good agreement, and the maximum relative error between the calculation values and the experimental data is less than 3.1%.

To reduce the influence of the smooth Coulomb friction during the dynamic stiffness test, it is necessary to use the low amplitude signals as much as possible. The dynamic stiffness tests were conducted with the excitation frequencies range from 2 to 100 Hz, the interval of 2 Hz, and the amplitude of 0.05 mm. Then, the contribution of the FDKVM to the dynamic stiffness of the RIP can be obtained. The fractional derivative order a and the damping parameter b can be identified by using the least square method. According to Equations (2), (24), and (26), the material parameter β also can be identified. These parameters of the SCFM and the FDKVM are shown in Table 6.

When the amplitude of the RIP is 0.05 mm, the calculated and experimental curves of the dynamic stiffness and the loss factor are shown in Figure 14. According to Figure 14, it can be observed that the dynamic stiffness and the loss factor of the RIP with or without thermal oxygen aging increases as excitation frequency increases. However, the dynamic stiffness with the thermal oxygen aging is higher than that without thermal oxygen aging, and the maximum growth rate of the dynamic stiffness is 4.5%. Simultaneously, compared with the RIP without thermal oxygen aging, the maximum decrease rate of the loss factor

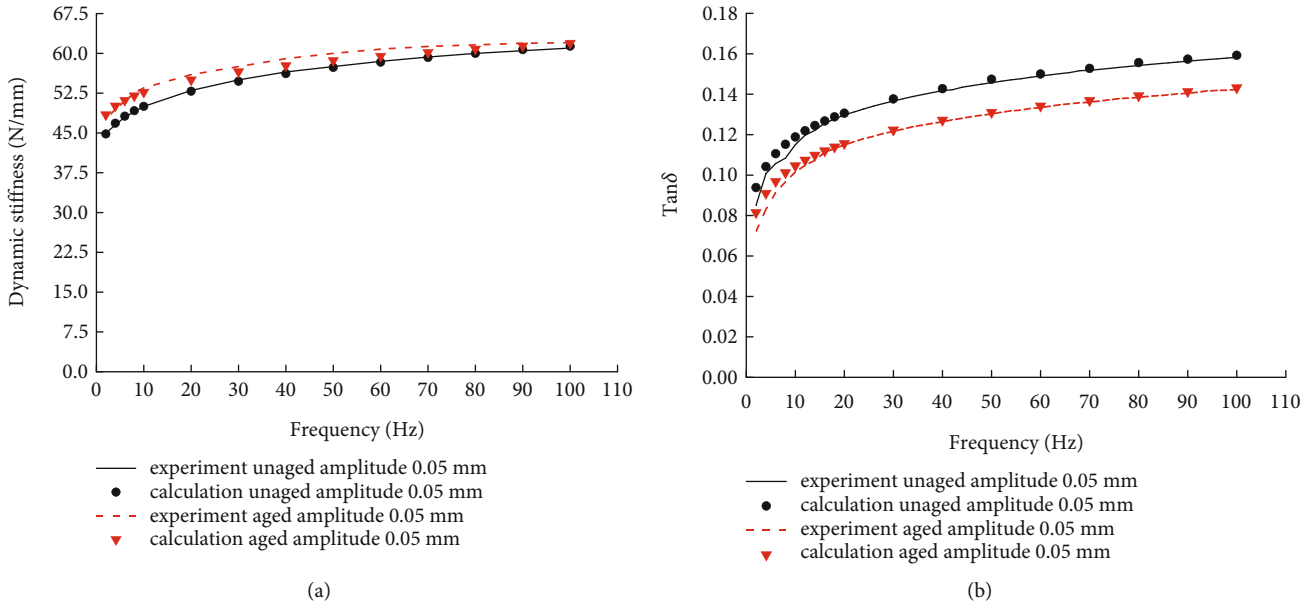

Figure 14: Dynamic stiffness and loss factor under the amplitude of 0.05 mm. (a) Dynamic stiffness with or without thermal oxygen aging, and (b) loss factor with or without thermal oxygen aging.

is 10.6%. The relative errors between the calculation values and the experimental data of the dynamic stiffness and the loss factor are less than 2.3%, 2.9%, respectively.

4.2. Model Validation. For further verifying the validity of thermal oxygen aging-dynamic characteristic model, the static stiffness tests with a velocity of 10 mm/min, and the amplitudes of 0.2 and 0.5 mm were performed by the MTS831, the hysteresis loops of the static stiffness with or without the thermal and oxygen aging of the RIP are shown in Figure 15. It can be seen from Figure 15 that although the model parameters were identified by adopting the experimental data with the amplitude of 1 mm, the identified parameters can accurately reproduce the hysteresis characteristic under the amplitudes of 0.2 and 0.5 mm. Therefore, the thermal oxygen aging-dynamic characteristic model can accurately characterize the hysteresis characteristic of the RIP with or without the thermal oxygen aging at the different amplitudes, and the static stiffness of the RIP with the thermal oxygen aging at the different amplitudes increases significantly. It also shows that it is indispensable to introduce the thermal oxygen aging dependence of the RIP.

To further analyze the effect of the thermal oxygen aging on the static stiffness of the RIP, the hysteresis loops with or without the thermal oxygen aging are shown in Figure 16 when the loading speed is 10 mm/min and the amplitudes are 0.2, 0.5, and 1 mm, respectively.

From Figure 16, the slope of the curves goes down with the increase in the amplitude, so the static stiffness gradually decreases. Consequently, the static stiffness of the RIP decreases with the increase of the amplitude, and the variation of the static stiffness is nonlinear, so the nonlinear relationship is characterized by the hyperelastic model. At the same time, the inclination of the curves becomes steeper with the thermal oxygen aging, then the static stiffness becomes larger. The increase of the static stiffness with the thermal oxygen aging is 20.7%, which will generate greater vibration and noise in the compressor and corresponding piping system.

To study the influence of the thermal oxygen aging on the amplitude dependence and the frequency dependence of the dynamic characteristic, a sinusoidal excitation with the amplitudes of 0.2 and 0.5 mm, the frequency range of 2–100 Hz, and an interval of 2 Hz were applied to test the dynamic stiffness of the RIP with or without the thermal oxygen aging. The calculated curves and experimental curves of the dynamic stiffness and the loss factor are shown in Figure 17. From Figure 17, it can be found that the identified parameters with the amplitude of 0.05 mm can also reproduce the dynamic stiffness characteristic and the loss factor with the amplitudes of 0.2 and 0.5 mm, respectively. It shows that the thermal oxygen aging-dynamic characteristic model can accurately describe the change laws of the dynamic stiffness and the loss factor of the RIP with or without the thermal oxygen aging.

Figure 17 depicts that the dynamic stiffness of the RIP with the thermal oxygen aging under the different amplitudes all show an increasing trend, and the loss factor shows a decreasing trend compared with that without the thermal oxygen aging. The vibration isolation and the damping performance of the RIPs are degraded, which further causes the vibration of the compressor and the noise to increase.

From Figure 17, as the frequency continues to increase, the slopes of the dynamic stiffness curves and the loss factor curves continue to decrease, which shows that the growth of the dynamic stiffness and the loss factor tends to be flat. The frequency dependence of the dynamic stiffness and the loss factor of the RIPs with the thermal oxygen aging is similar to that without the thermal oxygen aging. When the frequency is in the low-frequency range of 0–20 Hz, the

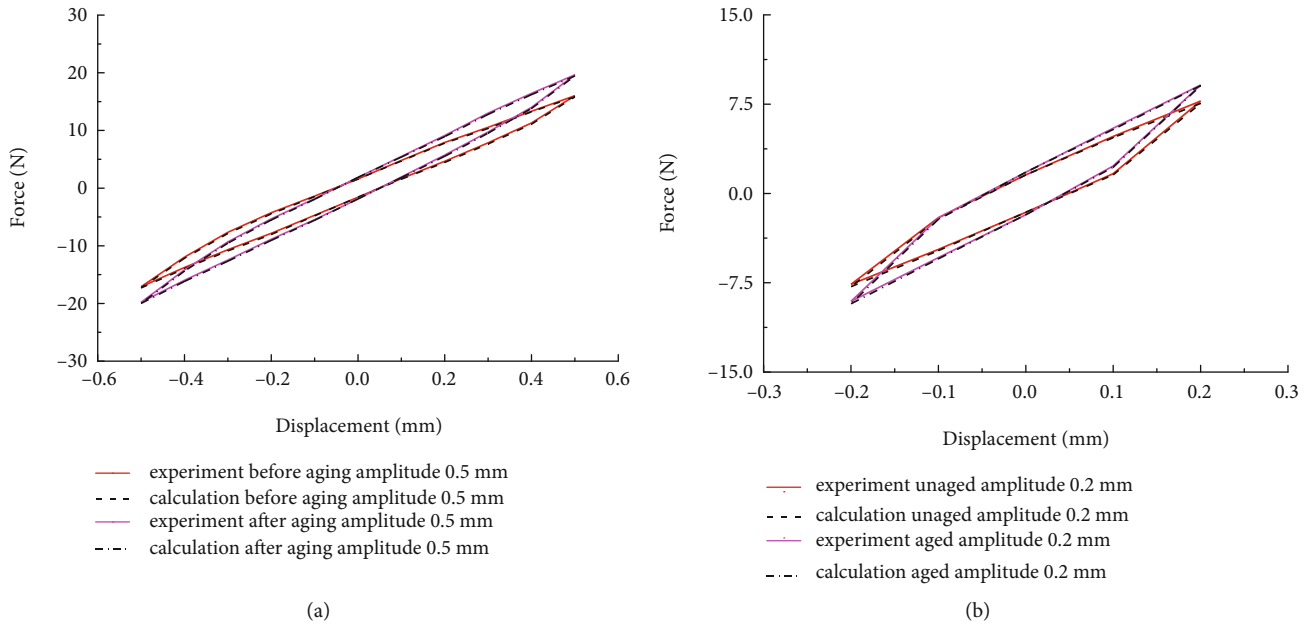

Figure 15: Hysteresis loops under the amplitudes of 0.2 and 0.5 mm. (a) Hysteresis loops under the amplitude of 0.5 mm, and (b) hysteresis loops under the amplitude of 0.2 mm.

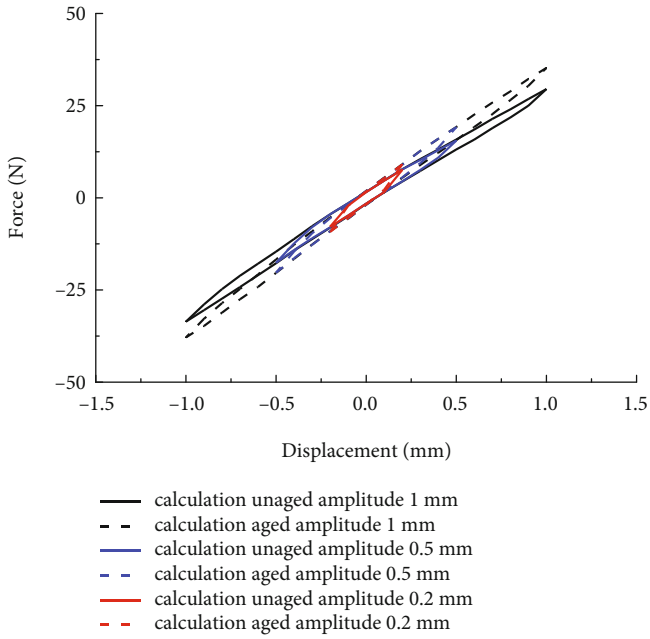

Figure 16: Hysteresis loops under the different amplitudes.

frequency has a greater influence on the dynamic stiffness and the loss factor. The low-frequency operation of the compressor is mainly in the start-stop phase, and the amplitude of the low-frequency operation is generally larger, which is easy to damage the pipeline. For the common inverter air conditioners, the compressor is frequently started and stopped. If the stiffness of the original RIPs is matched reasonably, the thermal oxygen aging will destroy the original matching rationality and the loss factor is reduced. These will increase the compressor vibration, further affect the reliability of the pipeline, and increase the noise.

Similarly, when the compressor runs to the middle- and the high-frequency above 20 Hz, the influence of the thermal oxygen aging will also increase the vibration of the compressor. But as the frequency increases, the growth of the dynamic stiffness and the loss factor shows a relatively flat growth, then the frequency dependence gradually weakens. Especially if the frequency is greater than 70 Hz, the influence of the thermal oxygen aging will become the leading factor in aggravating the vibration of the compressor.

From Figure 18, the dynamic stiffness and the loss factor of the RIP increase as the frequency increases under the same amplitudes. Under the same frequency range, the dynamic stiffness of the RIP decreases with the increase of the amplitude, but the loss factor increases with the increase of the amplitude.

Actually, the RIPs will undergo side-group oxygen reaction under the combined action of the thermal oxygen environment and the vulcanization system, and the internal molecular chains will be further cross-linked [41], and the cross-linking density increases, then the more stable C–C cross-link bond is formed. The anti-aging system of the rubber formula captures and combines free oxygen and the rubber free radicals under the high temperature or the thermal oxygen aging conditions and reduces the degradation rate of rubber molecules. The aging of the RIP is dominated by the cross-linking, the combined effect of the cross-linking and the hardening of rubber under the thermal oxygen environment and the reduction of the degradation rate jointly give rise to the increase in the static stiffness of the RIP [42, 43]. The static stiffness data with the thermal oxygen aging at the temperature of 120°C and an amplitude of 1 mm were used to clarify the changes in the internal molecular structure of the EPDM, which is shown in Figure 19. From Figure 19, the rubber group undergoes the oxidation reaction to generate peroxide free radicals and combines

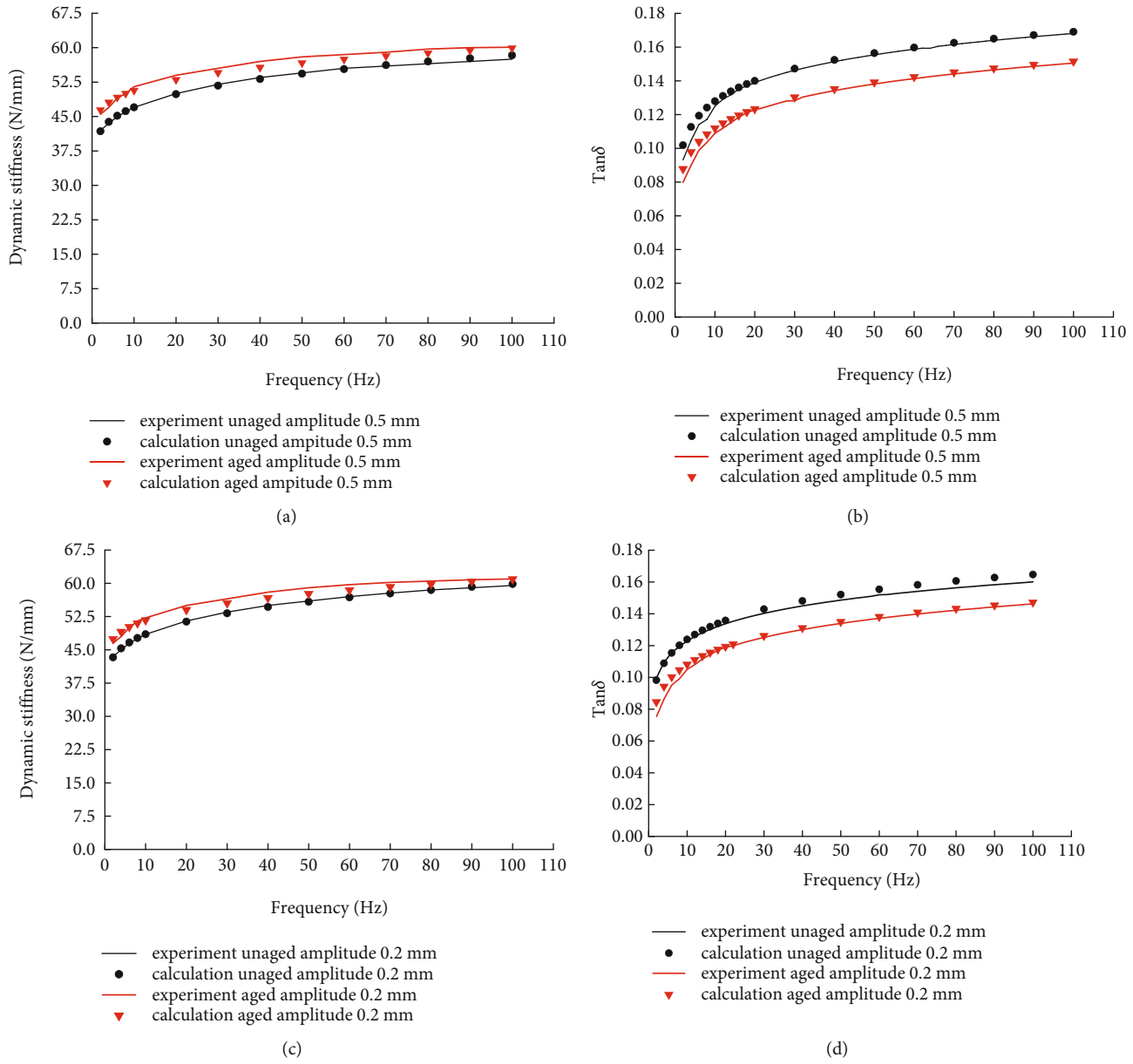

Figure 17: Dynamic stiffness and loss factor of the RIP under the different amplitudes. (a) Dynamic stiffness under the amplitude of 0.5 mm, (b) loss factor under the amplitude of 0.5 mm, (c) dynamic stiffness under the amplitude of 0.2 mm, and (d) loss factor under the amplitude of 0.2 mm.

with long-chain free radicals P to generate ethers, which indicates that a cross-linking reaction has occurred. The stiffness increases slowly for the first 16 hours and then increases dramatically from 16 to 24 hours. The oxidation of the polymers normally leads to an increase in the cross-linking density due to the introduction of the higher-density oxidation groups with time, which finally results in an increase in the static stiffness. Combining Equations (12), (19), (25), and (30), it can be found that the dynamic stiffness will also increase with the increase in the static stiffness.

The new model established in this paper can predict the dynamic characteristic of the RIP under the thermal oxygen environment and provides a theoretical basis for the stiffness matching and the optimization of the RIP. When the RIP is optimally matched with the compressor, the change of the static stiffness under the thermal oxygen aging conditions will destroy the reasonableness of the performance matching of the RIP and the compressor, which will produce the deterioration of the vibration isolation performance of the RIP. Therefore, the initial stiffness of the RIP can be adjusted appropriately; the stiffness of the RIP can be designed to be a little bit less than the optimal matching stiffness within the acceptable performance range. As the RIP will age under the thermal oxygen aging condition after a period of use, the optimal matching stiffness will be reached, which indirectly extends the service life of the RIP and optimizes the performance matching design of the RIP.

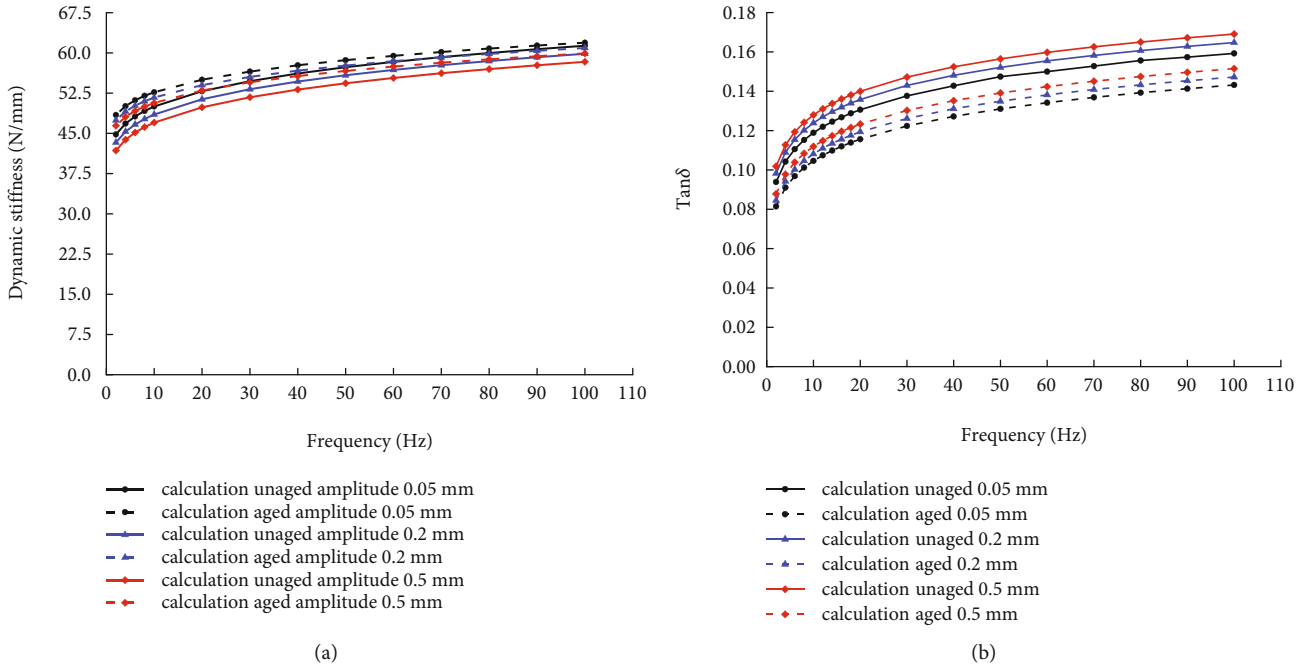

Figure 18: Calculation values of the dynamic stiffness and the loss factor of the RIP at the different amplitudes. (a) Calculation values of the dynamic stiffness and (b) calculation values of the loss factor.

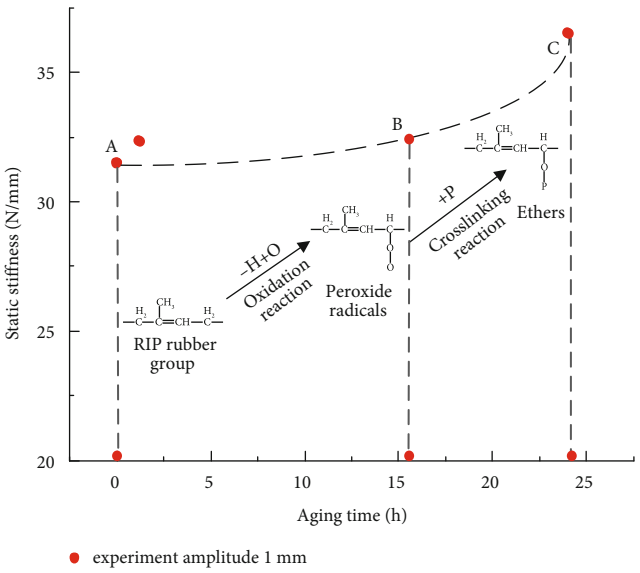

Figure 19: The changes in the internal molecular structure and the static stiffness.

In summary, the thermal oxygen aging of the RIP mainly changes the cross-linking density of the rubber material. With the thermal oxygen aging process, the cross-linking density of the EPDM increases, and the static stiffness becomes larger, which also makes the dynamic stiffness to increase, which is not conducive to the vibration isolation. Moreover, the loss factor of the RIP also shows a decreasing trend with the thermal oxygen aging, and the damping effect declines.

5. Conclusions

In this paper, the Peck model, the FDKVM, and the SCFM are introduced to establish the mathematical model of thermal oxygen aging-dynamic characteristic of the RIP, then the identification methods of the model parameters are given. The modeling method of the dynamic characteristic of the RIP is further developed and enriched in this study.

The results show that the relative error of the static stiffness, the dynamic stiffness, and the loss factor between the calculation values and the experimental data with or without the thermal oxygen aging are less than 3.1%, 2.3%, and 2.9%, respectively. It can be found that the novel model can accurately describe the hysteresis characteristic, the amplitude dependence, the frequency dependence, and the thermal oxygen aging dependence of the RIP.

Due to the change in the cross-linking density of the rubber molecular chain under the thermal oxygen aging condition, the maximum growth rate of the static stiffness and the dynamic stiffness is 20.7% and 4.5%, respectively. The maximum decrease rate of the loss factor is 10.6%. The thermal oxygen aging-dynamic characteristic model can describe the change law of the dynamic characteristic of the RIP and provides a good foundation for an in-depth study of the variation of the dynamic characteristic.

Next research will proceed to improve the dynamic characteristic model of the RIP under the different thermal oxygen aging processes. This research is only applicable when the thermal oxygen aging mechanism of the RIP is almost consistent. When the aging process is inconsistent due to the gradual change in the temperature, the thermal oxygen aging-dynamic characteristic model will need to be further refined based on this study in this paper.

Notations

HA: Shore hardness
C_1, C_2: Acceleration coefficients associated with thermal oxygen aging
E_a: Activation energy of the reaction
R: Molar gas constant
T: Kelvin temperature
t: Thermal oxygen aging time
μ: Thermal oxygen aging factor
β: The material parameter
I_1, I_2, I_3: Strain invariants
C_{ij}, d_k, N: Material constants
t_{ij}: Kirchhoff stress tensor
γ_{ij}: Green strain tensor
t_i: Principal stress
λ_i: Principal elongation ratio
P: Arbitrary hydrostatic pressure
C_{10}, C_{01}, D_1: The material parameters of the Mooney–Rivlin constitutive model
a: Fractional derivative order
b: Fractional derivative damping parameter
D^a: Fractional differential form
F_{fs}: Reference frictional force
F_{fmax}: Maximum frictional force
x_s: Reference displacement
x_0: Displacement amplitude
x_2: Friction displacement when the frictional force equals $F_{fmax}/2$
K_{he}: Equivalent elastic stiffness
K_e: Linear elastic stiffness
K_c: Correction stiffness
K_v: The dynamic stiffness of the FDKVM
K_f: The stiffness of the SCFM
K_{vf}^*: Complex stiffness
K_{va}: The dynamic stiffness of the FDKVM with the thermal oxygen aging
K_{fa}: The stiffness of the SCFM with the thermal oxygen aging
K_{vfa}^*: The complex stiffness with the thermal oxygen aging
$\tan\delta$: Loss factor
$\tan\delta_a$: The loss factor with the thermal oxygen aging.

Data Availability

Data supporting this research article are available from the corresponding author or first author upon reasonable request.

Conflicts of Interest

The authors declare that they have no conflicts of interest.

Acknowledgments

The authors express thanks sincerely to Jingfeng Fang and Weizhong Wang, Bonderra Industries Co., Ltd., for product design, manufacture and experiments and thanks sincerely to Dr Chaofeng Yang, Anhui Zhongding NVH Co., Ltd., for performing the experiments. The authors also thank sincerely the editors and the reviewers for their delicate work. The author(s) disclosed receipt of the following financial support for the research, authorship, and/or publication of this article: Authors would like to acknowledge the support by (1) National Natural Science Foundation of China (Project No. 51905240 for supporting the establishment of a dynamic characteristic model of the RIP), (2) Ganzhou Science and Technology Innovation Talents Project and Ganzhou Key R&D Project (Industrial Field) for supporting modeling and tests, and (3) Special Funds of the Central Government Guiding Local Science and Technology Development (Project No. 202007d06050015 for performing the static and dynamic stiffness tests).

References

[1] S. Sun, H. Deng, H. Du et al., "A compact variable stiffness and damping shock absorber for vehicle suspension," *IEEE/ASME Transactions on Mechatronics*, vol. 20, no. 5, pp. 2621–2629, 2015.

[2] C. Liu, X. Jing, S. Daley, and F. Li, "Recent advances in micro-vibration isolation," *Mechanical Systems and Signal Processing*, vol. 56–57, pp. 55–80, 2015.

[3] X. Sun and X. Jing, "A nonlinear vibration isolator achieving high-static-low-dynamic stiffness and tunable anti-resonance frequency band," *Mechanical Systems and Signal Processing*, vol. 80, pp. 166–188, 2016.

[4] Q. He, G. Wang, Y. Zhang, Z. Li, L. Kong, and W. Zhou, "Thermo-oxidative ageing behavior of cerium oxide/silicone rubber," *Journal of Rare Earths*, vol. 38, no. 4, pp. 436–444, 2020.

[5] M. Sugimoto, A. Shimada, H. Kudoh, K. Tamura, and T. Seguchi, "Product analysis for polyethylene degradation by radiation and thermal ageing," *Radiation Physics and Chemistry*, vol. 82, pp. 69–73, 2013.

[6] M. Raei and M. Dardel, "Tuned mass damper and high static low dynamic stiffness isolator for vibration reduction of beam structure," *Proceedings of the Institution of Mechanical Engineers Part K Journal of Multi-body Dynamics*, vol. 234, no. 1, pp. 95–115, 2019.

[7] E. Esmizadeh, G. Naderi, and M. Barmar, "Effect of organoclay on properties and mechanical behavior of fluorosilicone rubber," *Fibers & Polymers*, vol. 15, no. 11, pp. 2376–2385, 2014.

[8] P. M. Subhani and R. K. Kumar, "A new stored energy function for rubber like materials for low strains," *Mechanics of Advanced Materials and Structures*, vol. 16, no. 5, pp. 402–416, 2009.

[9] M. Kamiński and B. Lauke, "Probabilistic and stochastic aspects of rubber hyperelasticity," *Meccanica*, vol. 53, no. 9, pp. 2363–2378, 2018.

[10] B. Kim, S. B. Lee, J. Lee et al., "A comparison among neo-Hookean model, Mooney-Rivlin model, and Ogden model for chloroprene rubber," *International Journal of Precision Engineering & Manufacturing*, vol. 13, no. 5, pp. 759–764, 2012.

[11] N. Kaya, M. Y. Erkek, and C. Güven, "Hyperelastic modelling and shape optimisation of vehicle rubber bushings," *International Journal of Vehicle Design*, vol. 71, no. 1/2/3/4, pp. 212–225, 2016.

[12] D. M. Oza and A. Londhe, "CAE simulation approach to predict behavior of hyper-elastic (rubber) material," *SAE Technical Paper*, vol. 1, no. 403, pp. 1–5, 2016.

[13] R. Han, Y. Wu, and X. Quan, "Effects of crosslinking densities on mechanical properties of nitrile rubber composites in thermal oxidative aging environment," *Journal of Applied Polymer Science*, vol. 137, no. 36, pp. 1–10, 2020.

[14] T. Yang, Y. Zhao, H. S. Liu, and S. Xiong, "Effect of sizing agents on surface properties of T800 Grade CF and thermal aging time on mechanical properties of T800 Grade CF/epoxy composites," *International Journal of Polymer Science*, vol. 2021, p. 9, 2021.

[15] S. Nie, J. Lacayo-Pineda, N. Willenbacher, and M. Wilhelm, "Aging of natural rubber studied via Fourier-transform rheology and double quantum NMR to correlate local chain dynamics with macroscopic mechanical response," *Polymer*, vol. 181, pp. 1–12, 2019.

[16] A. R. Azura and S. L. Leow, "Effect of carbon black loading on mechanical, conductivity and ageing properties of natural rubber composites," *Materials Today: Proceedings*, vol. 17, pp. 1056–1063, 2019.

[17] S. K. Loh, W. F. Faris, M. Hamdi, and W. M. Chin, "Vibrational characteristics of piping system in air conditioning outdoor unit," *SCIENCE CHINA Technological Sciences*, vol. 54, no. 5, pp. 1154–1168, 2011.

[18] M. Sjöberg and L. Kari, "Non-Linear behavior of a rubber isolator system using fractional derivatives," *Vehicle System Dynamics*, vol. 37, no. 3, pp. 217–236, 2002.

[19] W. Luo, B. Yin, X. Hu, Z. Zhou, Y. Deng, and K. Song, "Modeling of the heat build-up of carbon black filled rubber," *Polymer Testing*, vol. 69, pp. 116–124, 2018.

[20] Y. Hu, H. Zhu, W. D. Zhu, C. Li, and Y. Pi, "Dynamic performance of a multi-ribbed belt based on an overlay constitutive model of carbon-black-filled rubber and experimental validation," *Mechanical Systems and Signal Processing*, vol. 95, pp. 252–272, 2017.

[21] J. J. Chen, Z. H. Yin, and S. Rakheja, "Theoretical modelling and experimental analysis of the vertical stiffness of a convoluted air spring including the effect of the stiffness of the bellows," *Proceedings of the Institution of Mechanical Engineers, Part D: Journal of Automobile Engineering*, vol. 232, no. 4, pp. 547–561, 2018.

[22] J. J. Chen, Z. H. Yin, X. J. Yuan, G. Q. Qiu, K. H. Guo, and X. L. Wang, "A refined stiffness model of rolling lobe air spring with structural parameters and the stiffness characteristics of rubber bellows," *Measurement*, vol. 169, pp. 1–14, 2021.

[23] W. Thaijaroen and A. J. L. Harrison, "Nonlinear dynamic modelling of rubber isolators using six parameters based on parabolic spring, springpot, and smooth-slip friction element," *Polymer Testing*, vol. 29, no. 7, pp. 857–865, 2010.

[24] C. O. Rodas, F. Zaieri, and M. Naiet-Abdelaziz, "A finite strain thermo-viscoelastic constitutive model to describe the self- heating in elastomeric materials during low-cycle fatigue," *Journal of the Mechanics and Physics of Solids*, vol. 64, pp. 396–410, 2014.

[25] J. Zhi, Q. Wang, M. Zhang, M. Li, and Y. Jia, "Coupled analysis on heterogeneous oxidative aging and viscoelastic performance of rubber based on multi-scale simulation," *Journal of Applied Polymer Science*, vol. 136, no. 18, pp. 1–10, 2019.

[26] B. Moon, N. Jun, and S. Park, "A study on the modified Arrhenius equation using the oxygen permeation block model of crosslink structure," *Polymers*, vol. 11, no. 1, pp. 1–15, 2019.

[27] V. Le Saux, P. Y. Le Gac, and Y. Marco, "Limits in the validity of Arrhenius predictions for field ageing of a silica filled polychloroprene in a marine environment," *Polymer Degradation and Stability*, vol. 99, pp. 254–261, 2014.

[28] W. Zheng, X. Zhao, Q. Li, T. W. Chan, L. Zhang, and S. Wu, "Compressive stress relaxation modeling of butadiene rubber under thermo-oxidative aging," *Journal of Applied Polymer Science*, vol. 134, no. 12, pp. 1–8, 2017.

[29] E. V. Bystritskaya, A. L. Pomerantsev, and O. Y. Rodionova, "Evolutionary design of experiment for accelerated aging tests," *Polymer Testing*, vol. 19, no. 2, pp. 221–229, 2000.

[30] Q. Liu, W. Shi, Z. Chen, K. Li, H. Liu, and S. Li, "Rubber accelerated ageing life prediction by peck model considering initial hardness influence," *Polymer Testing*, vol. 80, pp. 1–10, 2019.

[31] N. Nosrati, A. Zabett, S. Sahebian et al., "Stress dependency of creep response for glass/epoxy composite at nonlinear and linear viscoelastic behavior," *International Journal of Polymer Science*, vol. 2022, p. 11, 2022.

[32] M. Sjöberg and L. Kari, "Nonlinear isolator dynamics at finite deformations: an effective hyperelastic, fractional derivative generalized friction model," *Nonlinear Dynamic*, vol. 33, no. 3, pp. 323–336, 2003.

[33] I. S. Liu, "A note on the Mooney–Rivlin material model," *Continuum Mechanics and Thermodynamics*, vol. 24, no. 4–6, pp. 583–590, 2012.

[34] M. Berg, "A model for rubber springs in the dynamic analysis of rail vehicles," *Proceedings of the Institution of Mechanical Engineers Part F: Journal of Rail and Rapid Transit*, vol. 211, no. 2, pp. 95–108, 1997.

[35] Technical Committee ISO/TC 45, Rubber and rubber products, Subcommittee SC 2, Testing and analysis, *ISO 37: 2005, Rubber, Vulcanized or Thermoplastic-Determination of Tensile Stress–Strain Properties*, International Standard Organization, Switzerland, 2005.

[36] Technical Committee ISO/TC 45, Rubber and rubber products, Subcommittee SC 2, Testing and analysis, *ISO 188-2011, Rubber, Vulcanized or Thermoplastic- Accelerated Aging and Heat Resistance Tests*, International Standard Organization, Switzerland, 2011.

[37] Technical Committee ISO/TC 45, Rubber and rubber products, Subcommittee SC 2, Testing and analysis, *ISO 7619-1: 2010, Rubber, Vulcanized or Thermoplastic- Determination of Indentation Hardness-Part 1: Durometer Method (Shore Hardness)*, Switzerland, International Standard Organization, 2010.

[38] M. Celina, K. T. Gillen, and R. A. Assink, "Accelerated aging and lifetime prediction: Review of non-Arrhenius behaviour due to two competing processes," *Polymer Degradation and Stability*, vol. 90, no. 3, pp. 395–404, 2005.

[39] Q. Liu, W. Shi, and Z. Chen, "Natural environment degradation prediction of rubber and MPSO-based aging acceleration factor identification through the dispersion coefficient minimisation method," *Polymer Testing*, vol. 77, pp. 105884–105886, 2019.

[40] M. Berg, "A non-linear rubber spring model for rail vehicle dynamics analysis," *Vehicle System Dynamics*, vol. 30, no. 3–4, pp. 197–212, 1998.

[41] X. Liu, J. Zhao, R. Yang, R. Iervolino, and S. Barbera, "Effect of lubricating oil on thermal aging of nitrile rubber," *Polymer Degradation and Stability*, vol. 151, pp. 136–143, 2018.

[42] R. A. Assink, K. T. Gillen, and B. Sanderson, "Monitoring the degradation of a thermally aged EPDM terpolymer by ^{1}H NMR relaxation measurements of solvent swelled samples," *Polymer*, vol. 43, no. 4, pp. 1349–1355, 2002.

[43] H. W. Chou, J. S. Huang, and S. T. Lin, "Effects of thermal aging on fatigue of carbon black–reinforced EPDM rubber," *Journal of Applied Polymer Science*, vol. 103, no. 2, pp. 1244–1251, 2007.